

Unexpected Hydride: $\text{Ce}_4\text{B}_2\text{C}_2\text{H}_{2.42}$, a Stuffed Variant of the Nd_2BC Structure Type

Mary B. Hertz, Ryan Baumbach, Xiaoping Wang, and Susan E. Latturmer*

Cite This: *Cryst. Growth Des.* 2021, 21, 5164–5171

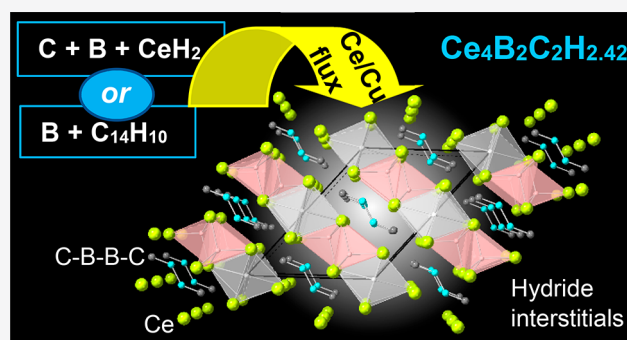
Read Online

ACCESS |

Metrics & More

Article Recommendations

ABSTRACT: $\text{Ce}_4\text{B}_2\text{C}_2\text{H}_{2.42}$ was grown as large crystals from a cerium/copper eutectic flux. The structure was characterized by single-crystal X-ray and neutron diffraction and was found to be a stuffed variant of Nd_2BC with the addition of two interstitial hydrogen positions. The tetrahedral hydrogen position is fully occupied, while the octahedral position has an occupancy of 42(3)%. Initial synthesis was due to hydrogen contamination of the cerium metal but has been successfully repeated using anthracene as a carbon and hydrogen source. Density of states calculations suggest that the incorporation of hydrogen stabilizes the compound with respect to the nonhydrided model. Magnetic susceptibility data show a complex magnetic ordering at 7.7 K that originates from the localized electron on the Ce^{3+} in the structure. The trivalent state is also supported by X-ray photoelectron spectroscopy measurements. Heat capacity and electrical resistivity data show that the phase transition is broad in temperature, which may be due to structural disorder. The large low temperature value of C/T also indicates possible heavy fermion behavior.



INTRODUCTION

Rare earth borocarbides have been a topic of ongoing interest over the last several decades due to the wide variety of complex structure types and properties these materials display. The arrangements of rare earth ions in these structures—such as two-dimensional nets^{1–3} or one-dimensional chains⁴—can lead to unusual magnetic behavior. There also exists a broad range of boron and carbon environments in these structures, from isolated atoms surrounded by rare earth ions, to borocarbide chains of various lengths and configurations (for instance, $\text{La}_{15}\text{B}_{14}\text{C}_{19}$ contains two types of 11-member borocarbide chains), to planes and nets of boron and carbon as seen in LaB_2C_2 .^{5,6}

Because of the high melting point of boron and carbon, these compounds are commonly synthesized by arc melting reagents together, followed by lengthy annealing of the sample. Metal flux synthesis offers an alternative method that enables shorter, lower temperature reactions compared to traditional approaches. This is a solution-based method, allowing for crystal growth of products. A low-melting combination of a rare earth and late transition metal has been shown to be an excellent solvent for refractory species, as demonstrated by the synthesis of $\text{Ce}_{10}\text{Co}_{2.64}\text{B}_{11.70}\text{C}_{10}$, $\text{Pr}_6\text{Co}_5\text{Ge}_{1+x}\text{Al}_{3-x}$, $\text{Nd}_8\text{Co}_{4-x}\text{Al}_x\text{Ge}_2\text{C}_3$, and $\text{La}_{21}\text{Fe}_8\text{Sn}_7\text{C}_{12}$.^{7–10} Given the fact that the rare earth is often incorporated into the flux-grown products, cerium-based eutectics are particularly appealing for use as metal fluxes. Cerium can exhibit mixed valences, with

both the (III) and (IV) states accessible, as seen in $\text{CeNi}_2\text{B}_2\text{C}$.¹¹ It is also commonly seen that strong hybridization between the *f*- and conduction electron states often leads to Kondo lattice physics and heavy fermion behavior.^{12,13} Compounds such as CeCoIn_5 and CeRu_3Si_2 display unconventional superconductivity,^{14,15} sometimes simultaneously with magnetic behavior as seen in $\text{Ce}_3\text{PdIn}_{11}$.¹⁶ In many of these materials, the superconductivity is found to emerge when a magnetically ordered state is continuously suppressed toward zero temperature at a quantum critical point,^{17,18} and a complete theory for such behavior remains to be established. As a result, Ce-based intermetallics continue to be intensely investigated for their novel properties and potential contribution to fundamental topics.

In this work, reactions in cerium/copper melts were explored for the synthesis of cerium borocarbides. The cerium–copper phase diagram features a eutectic point at 72 mol % cerium to 28 mol % copper that melts at 424 °C, far below the melting point of either constituent. Copper was

Received: May 4, 2021

Revised: July 19, 2021

Published: July 29, 2021



chosen as a promising transition metal component primarily for its propensity to solubilize boron,¹⁹ but it is also attractive that (i) copper tends to have no magnetic contribution in intermetallic systems, thereby allowing sole focus on the magnetic behavior of the cerium and (ii) hybridization effects can be strong in such materials, as exemplified by the heavy fermion superconductor CeCu₂Si₂.^{20,21} Carbon and boron were reacted in a near-eutectic composition Ce/Cu (74 mol % Ce, 26 mol % Cu, mp 440 °C) to form a new cerium borocarbide. Because of the large excess of flux used for these reactions, any contaminants of the flux reagents have the potential to incorporate into the crystallized products. This has been observed in several metal hydride compounds grown from calcium-rich fluxes including LiCa₂C₃H, LiCa₇Ge₃H₃, and Ca₃SiN₃H.^{22–24} Similar behavior is noted here. As a result of cerium hydride contaminant in the cerium-rich flux, Ce₄B₂C₂H_{2.42} was isolated; this is a stuffed variant of the Nd₂BC structure in which hydride interstitials are incorporated. The presence and siting of the hydrides were verified by single-crystal neutron diffraction and reproduced in reactions using anthracene as both a carbon and hydrogen source. The electronic and magnetic behavior were investigated with magnetic susceptibility, resistivity, and heat capacity measurements, as well as density of states calculations comparing hydrided and nonhydrided models.

■ EXPERIMENTAL PROCEDURES

Synthesis. Ce₄B₂C₂H_{2.42} was grown from the reaction of cerium (99%, Acros, chunks) and copper (99.5%, Alfa Aesar, powder) with elemental boron (99.4%, Strem Chemicals, crystalline) and carbon (99.99%, Strem Chemicals, acetylene black powder). These elements were combined in a Ce/Cu/B/C ratio of 7.4:2.6:1:1 mmol in an alumina crucible. Refractory elements boron and carbon were added first, followed by copper. Cerium pieces were placed on top; as the lowest melting component, it will melt first and react with the copper to form the flux, which will then dissolve the boron and carbon. Since carbon and boron are both nonvolatile refractory materials that are physically separated from the cerium, there is no way for them to come into physical contact with the cerium in order to react until the melt forms. It is essential to avoid an initial reaction between cerium and these refractory elements since the Ce/B or Ce/C binaries that would be formed could prevent any further reaction from occurring. The crucible was placed into a fused silica tube with a wad of quartz wool above it. The tube was then flame-sealed under a vacuum. The ampule was heated to 1000 °C in 3 h, maintained at 1000 °C for 6 h, cooled to 850 °C in 24 h, held at 850 °C for 18 h, and finally cooled to 550 °C in 96 h. At this temperature, it was removed from the furnace, inverted, and centrifuged to strip excess flux away from the products. The title phase reacts with moist air and was therefore stored either in a nitrogen flow-through desiccator or in an argon-filled glovebox to prevent oxidation. Elemental analyses were carried out using a FEI NOVA 400 scanning electron microscope with energy-dispersive spectroscopy capabilities. Product crystals were placed on a sample puck with carbon tape and cleaved to expose interior areas to avoid spurious readings due to flux residue on the sample surface. Because of the limitations of this technique toward light elements, only cerium was detected in the samples. No incorporation of copper from the flux or aluminum from the crucible was seen.

It is notable that a metal hydride was produced despite the fact that there was no hydrogen source deliberately added to the reaction. It is likely that the cerium metal reactant was contaminated with CeH_x, allowing for the formation of the title phase. In order to test this assumption, ingots of a Ce/Cu mixture were each prepared by arc melting 7.4 mmol Ce + 2.6 mmol Cu. The high temperature of this process (arc melting the mixture several times under argon with intermittent flipping of the resulting button to ensure mixing of the

metals) will decompose and remove any hydride contaminant. When carbon and boron were reacted in this arc-melted Ce/Cu flux using the same heating profile mentioned above, the title phase was not produced. On the other hand, when 1 mmol of elemental boron and 0.1 mmol of anthracene (C₁₄H₁₀, 97%, Sigma-Aldrich, reagent grade) were reacted in another piece of arc-melted Ce/Cu mixture, the title phase was obtained.

Diffraction Studies. Single-crystal samples that were clean of surface flux were selected and mounted onto cryoloops with paratone oil. This oil holds the crystals in place on the loop without contributing to the diffraction signal. Single-crystal X-ray diffraction (SC-XRD) data were collected at 200 K on a Bruker SMART APEX2 CCD diffractometer equipped with a Mo K α X-ray tube ($\lambda = 0.71073$ Å). The data sets were integrated with the SAINT program²⁵ and then corrected for absorption effects using the empirical method SADABS.²⁶ The structures were then solved using direct methods in order to locate cerium atoms, while positions of boron and carbon were found through the combined use of least-squares refinement and difference Fourier maps using the SHELX-97 software package.²⁷

Neutron diffraction studies were undertaken at Oak Ridge National Laboratory on BL-12 (TOPAZ).²⁸ A single crystal 1.15 mm \times 0.6 mm \times 0.49 mm was mounted onto a 1 mm MiTiGen tip and held in place with Krytox grease. Data were collected at 100 K using 25 crystal orientations determined using the CrystalPlan software for an estimated 99% coverage of reflections of the monoclinic cell.²⁹ Each orientation was exposed to the neutron beam until it had collected 20 C of charge, which required about 4 h of exposure at a nominal neutron beam power of 1.4 MW. The measurement was monitored by charge rather than exposure time due to normal fluctuations that can occur in the output power of the neutron beam. The integrated peak intensities were determined using the Mantid platform.³⁰ Data reduction (including detector efficiency, neutron TOF spectrum, and absorption corrections) was carried out using the ANVRED3 program.³¹ Details of the crystallographic data for the X-ray and neutron diffraction studies are shown in Table 1. Additional data are deposited in the CCDC with deposition number 2086224 for Ce₄B₂C₂H_{2.42}.

X-ray Photoelectron Spectroscopy. X-ray photoelectron spectroscopy (XPS) data were collected on Ce₄B₂C₂H_{2.42} to investigate the cerium valence. Cerium 3d core-line spectra were collected using a

Table 1. Crystallographic Data and Collection Parameters for Ce₄B₂C₂H_{2.42}

	X-ray diffraction	neutron diffraction
formula weight (g/mol)		608.59
crystal system		monoclinic
space group		C2/m (#12)
<i>a</i> (Å)	12.895(2)	12.895(3)
<i>b</i> (Å)	3.7661(6)	3.7661(6)
<i>c</i> (Å)	9.530(3)	9.530(2)
β (deg)	130.689(1)	130.688(1)
<i>Z</i>		2
volume (Å ³)	350.9(1)	350.9(1)
density, calc (g/cm ³)	5.755	5.7586
index ranges	−16 < <i>h</i> < 16 −4 < <i>k</i> < 5 −12 < <i>l</i> < 12	−18 < <i>h</i> < 17 −7 < <i>k</i> < 7 −17 < <i>l</i> < 18
reflections collected	2025	4086
temperature (K)	200(2)	100(2)
radiation	Mo K α ($\lambda = 0.71073$ Å)	neutron TOF
unique data/parameters	479/29	901/37
μ (mm ^{−1})	25.325	0.0200 + 0.4957 λ
<i>R</i> ₁ / <i>wR</i> ₂	0.0215/0.0561	0.0472/0.1188
<i>R</i> ₁ / <i>wR</i> ₂ (all data)	0.0231/0.0574	0.0507/0.1203
GOF	1.132	1.092

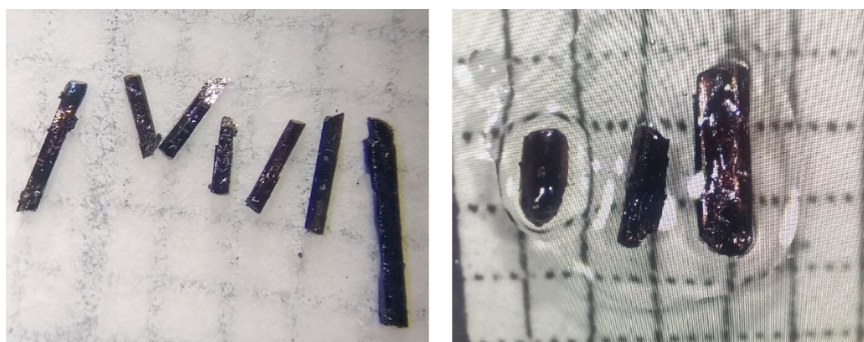


Figure 1. Microscope images of crystals of $\text{Ce}_4\text{B}_2\text{C}_2\text{H}_{2.42}$, taken on a millimeter grid background. Left: crystals grown from standard reaction. Right: crystals (in oil) grown from anthracene reaction.

Physical Electronics PHI 5100 series XPS with Al and Mg dual anode source and a single channel hemispherical energy analyzer. In these measurements, only the Al anode was used. Crystals were ground into a fine powder and spread over carbon tape on a gold sample puck. This sample was argon-sputtered incrementally for a total of 75 min to remove surface contaminants. The final Ce 3d data were collected as 15 sweeps from 930 to 875 at 0.100 eV/step, 250 ms/step, at a pass energy of 71.55 eV.

Magnetic Susceptibility and Electrical Transport Measurements. Magnetic susceptibility measurements were conducted on $\text{Ce}_4\text{B}_2\text{C}_2\text{H}_{2.42}$ single crystals to characterize the valence state of cerium and to detect possible magnetic ordering. Single crystals were selected from the product matrix and aligned on a piece of Kapton tape to position the long axis of the crystal (crystallographic *b*-axis) parallel to the applied field. This tape was then placed in a straw and then attached to the sample rod of a Quantum Design MPMS SQUID system. Magnetic susceptibility $\chi = M/H$ data were collected from 1.8–300 K under an applied magnetic field of $H = 2000$ Oe. Magnetization measurements at $T = 1.8$ K were also performed for $H < 7$ T. Electrical resistivity measurements for temperatures $T = 1.8$ –300 K were performed in a four-wire configuration using a Quantum Design Physical Property Measurement System. Platinum wires were spot-welded in place on the sample for this measurement and were positioned so that the electrical current runs along the *b*-axis of the crystal. Temperature-dependent heat capacity measurements were performed from 1.8–300 K using a Quantum Design PPMS using the thermal relaxation technique.

Electronic Structure Calculations. In order to calculate the density of states (DOS), cerium is modeled as lanthanum to avoid computational issues that stem from partially filled *f*-shells. The tight binding-linear muffin tin orbital-atomic sphere approximation (TB-LMTO-ASA) program package was used.³² Calculations were performed on three models: $\text{La}_4\text{B}_2\text{C}_2$ (no hydrides), $\text{La}_4\text{B}_2\text{C}_2\text{H}_2$ (tetrahedral hydride site fully occupied), and $\text{La}_4\text{B}_2\text{C}_2\text{H}_3$ (tetrahedral and octahedral hydride sites fully occupied). Calculations were based on unit cell parameters and atomic coordinates determined for $\text{Ce}_4\text{B}_2\text{C}_2\text{H}_{2.42}$ at 200 K by X-ray diffraction, with the exception of the hydride positions, which were determined by neutron diffraction studies. The following basis sets were used: La (6s, 5d, 4f), C (2s, 2p), B (2s, 2p), and H(1s), with La (6p), C (3d), and B (3d) being downfolded. Integration over the Brillouin zone was made by the tetrahedron method.³³

RESULTS AND DISCUSSION

Synthesis. Cerium metal is an attractive flux component due to its low melting point (800 °C), reactivity toward many elements, and complex electronic behavior. Reactions in cerium-rich eutectics (Ce/*T* where *T* = late transition metal such as Co, Ni, Cu) typically yield intermetallics that incorporate the cerium but not the transition metal. This observed trend is supported in the reactions studied here; the presence of copper lowers the melting point and may facilitate

the dissolution of boron and carbon, but no copper is found in the $\text{Ce}_4\text{B}_2\text{C}_2\text{H}_{2.42}$ product.

Incorporation of hydrogen was unexpected. The cerium metal is postulated to be the source of the hydrogen, for two reasons. The first is the observation that the yield of the title compound varied, ranging from 0 to 70% of the product matrix for different reactions, with the only difference being which piece of cerium metal was used. It is thought that certain lots of the metal from Acros may have had more hydrogen contamination, thereby leading to different amounts of hydrogen available to form the title phase. Given that lanthanide hydrides are a component of the rare earth metal production process, this seems plausible. Rare earth oxides obtained from ore are reduced to their metallic form by exposure of the material to a flow of H_2 gas, thereby reducing the oxide. Excess H_2 can be captured by the metal itself, forming a small amount of rare earth hydride.³⁴ To test this, reactions were carried out using a mixture of cerium and copper that was arc melted under argon before being placed in the reaction ampule. The high temperature of the arc melting process will decompose any cerium hydrides and will allow the cerium and copper to form the low-melting Ce/Cu mixture prior to use. This Ce/Cu prealloyed mixture was then added to an alumina crucible containing boron and anthracene ($\text{C}_{14}\text{H}_{10}$, both a carbon source and a deliberately added source of a controlled amount of hydrogen). This produced the title phase with even larger crystals seen from the original reaction. The overall yield of the reaction was consistent with well-performing batches of the original synthesis, with up to 70% of the product matrix belonging to the desired phase. It is notable that reactions of boron and carbon in the arc-melted Ce/Cu mixture do not produce the title phase, indicating the importance of the presence of hydrogen in stabilizing it.

$\text{Ce}_4\text{B}_2\text{C}_2\text{H}_{2.42}$ forms as silver rod crystals up to 3 mm in length and 0.25–0.50 mm in width; the wider crystals were formed from synthesis with anthracene (Figure 1). Most crystals are clean of visible flux, although traces of remaining flux could be scraped off the surface without fracture of the crystals. The crystals are air- and moisture-sensitive and readily oxidize but are stable in a nitrogen environment for several weeks.

Structure. The $\text{Ce}_4\text{B}_2\text{C}_2\text{H}_{2.42}$ phase is a stuffed variant of Nd_2BC in the *C2/m* space group and can be seen in Figure 2. As in the parent structure, this compound contains a [C–B–B–C] chain surrounded by rare-earth cations.³⁵ The siting of boron and carbon in this chain was assigned based on bond lengths and comparison to borocarbides with similar building blocks, including the previously reported Nd_2BC and

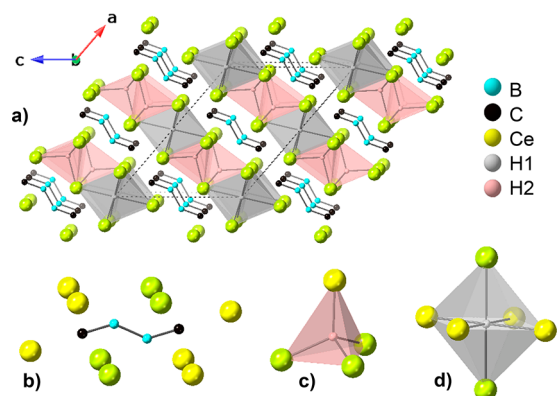


Figure 2. (a) The monoclinic structure of $Ce_4B_2C_2H_{2.42}$ viewed down the b -axis. Hydride positions shown in polyhedral mode. (b) Coordination environment of the borocarbide chain. (c) Tetrahedral interstitial hydride site. (d) Partially occupied octahedral interstitial hydride site.

$Ce_6Br_3B_2C_3$, in which the B–B distances were reported to be 1.65(2) Å and 1.64 Å, while the B–C distances were 1.51(2) Å and 1.53 Å, respectively.^{4,35} This is comparable with the B–B distance of 1.660(2) Å and the B–C distance of 1.506(1) Å observed for $Ce_4B_2C_2H_{2.42}$. Comparison of the unit cell parameters of $Ce_4B_2C_2H_{2.42}$ with those of the Nd_2BC structure show expansion along all axes, which is expected, as Ce^{3+} is larger than Nd^{3+} . Coordination distances around the rare earth cations also show the expected trend of Ce bond lengths as longer than those in the Nd compound. This points to the presence of trivalent cerium since the smaller radius of Ce^{4+} would be expected to lead to significantly shorter distances.

The possibility of the incorporation of a light atom on an interstitial site (suspected by the consistent appearance of a residual electron density peak on the $2a$ Wyckoff position in the electron density map in X-ray refinements of several different crystals) prompted the collection of neutron diffraction data. Hydrogen has a strong negative neutron scattering cross-section and is therefore easy to detect in neutron diffraction studies. While only one sample was studied by neutron diffraction (so there is uncertainty regarding possible $Ce_4B_2C_2H_x$ phase width), the data supported the presence of hydride in the $2a$ site, with an occupancy of 42%. This position is octahedrally coordinated by six cerium atoms, with Ce–H distances in the range of 2.798–2.941 Å. This compares well to the octahedral site distances of 2.765 Å seen in $CeH_{2.73}$.³⁶ The neutron diffraction data also clearly showed hydrides fully occupying a $4i$ Wyckoff position, which is a tetrahedrally coordinated interstitial site. The Ce–H distances of 2.437–2.470 Å to the four surrounding cerium ions are slightly larger than the 2.395 Å distance seen for tetrahedrally coordinated hydride sites in $CeH_{2.73}$.³⁶ The $4i$ -centered tetrahedra in $Ce_4B_2C_2H_{2.42}$ share edges; the resulting distance between the hydride ions is 2.766 Å, which is essentially the same value seen in the cerium hydride of 2.765 Å.³⁶

Cerium–cerium distances in the title phase range from 3.630(3)–4.152(3) Å, which exceeds the Hill limit of cerium (Ce–Ce distance of 3.4 Å). In general, the Hill limit gives an approximation for the minimum interatomic distance where the f -shells begin to overlap. At shorter distances, the shells overlap, and the f -electron tends to delocalize; this leads to nonmagnetic tetravalent cerium ions. If the cerium ions are further apart (as is the case here), the f -shells do not overlap, so the f -electron remains localized. This results in magnetic

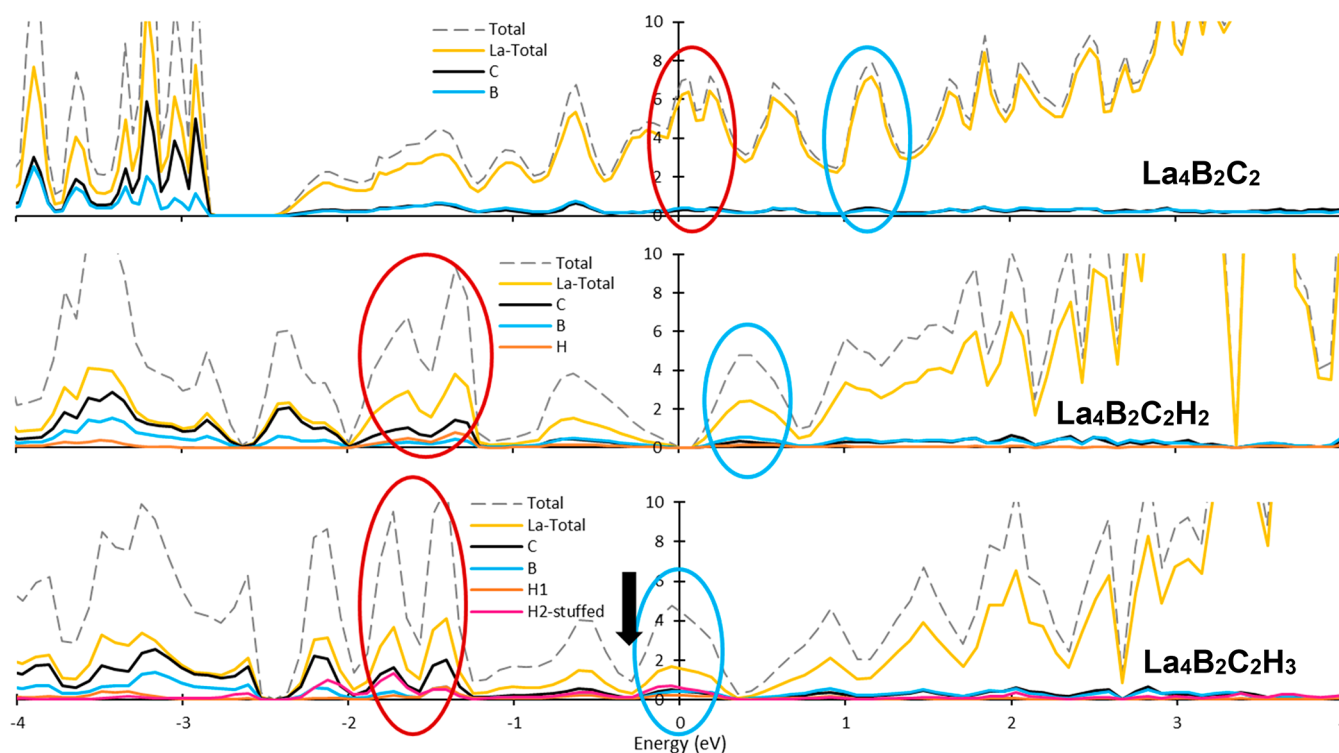


Figure 3. Density of states data for three models of the $Ce_4B_2C_2H_{2.42}$ structure. The Fermi level is set to 0 eV. Red and blue circles demonstrate the Fermi level shifting to higher energies with addition of more electrons. The black arrow indicates the likely true Fermi level for the material, accounting for partial occupancy of the $2a$ hydride site.

trivalent behavior.³⁷ Crucially, heavy fermion behavior that originates from Kondo lattice behavior is only observed in structures whose Ce–Ce distances are above the Hill limit.³⁸

Electronic Structure Calculations. Occupancy of the interstitial sites by hydride anions may serve to stabilize the structure. Density of states calculations were carried out for three models of the $\text{Ce}_4\text{B}_2\text{C}_2\text{H}_{2.42}$ compound: $\text{La}_4\text{B}_2\text{C}_2$ (this is analogous to the Nd_2BC structure), $\text{La}_4\text{B}_2\text{C}_2\text{H}_2$ (this has the $4i$ tetrahedral site occupied but the $2a$ octahedral site is unoccupied), and $\text{La}_4\text{B}_2\text{C}_2\text{H}_3$ (this has both the $4i$ and the $2a$ sites fully occupied). These models of the DOS are shown in Figure 3. The $\text{La}_4\text{B}_2\text{C}_2$ model shows the lanthanide states dominant at the Fermi level, indicating metallic behavior. The $\text{La}_4\text{B}_2\text{C}_2\text{H}_2$ model shows a very small band gap for the material, which is inconsistent with the measured resistivity results for this sample. The $\text{La}_4\text{B}_2\text{C}_2\text{H}_3$ model, on the other hand, does show electronic states present at the Fermi-level, thereby suggesting a metallic compound. However, the E_F is positioned at a peak in the DOS, which is in general considered destabilizing. Since this model assumes full occupancy of the $2a$ site (which is in fact partially occupied), the Fermi level will actually be shifted to a slightly lower value. The likely location is situated in a pseudogap that would tend to stabilize the structure. States corresponding to the hydride sites are seen from -1.2 to -2.5 eV. Consistent across all of the models are the states corresponding to the borocarbide chain, which are found well below E_F (from -2.5 to -4 eV).

The presence of hydride anions may also serve to bring $\text{Ce}_4\text{B}_2\text{C}_2\text{H}_{2.42}$ closer to a “charge-balanced” configuration. While charge balancing is rarely considered in intermetallic compounds due to the presence of delocalized conduction electrons, the Nd_2BC parent compound was postulated to contain an ionic borocarbide species $[\text{C}=\text{B}-\text{B}=\text{C}]^{8-}$ and the overall formula viewed as $(\text{Nd}^{3+})_4[\text{CBBC}]^{8-}\cdot 4e^-$.³⁵ The extra electrons were assumed to occupy Nd–Nd bonding states and antibonding π^* states in the $[\text{CBBC}]^{8-}$ unit. The presence of the interstitial hydride ions may account for some of the extra electrons required for charge balancing.

Magnetic Susceptibility. The temperature-dependent magnetic susceptibility $\chi = M/H$ data are shown in Figure 4. In the inset (Figure 4b), the data for $T > 150$ K are fitted to

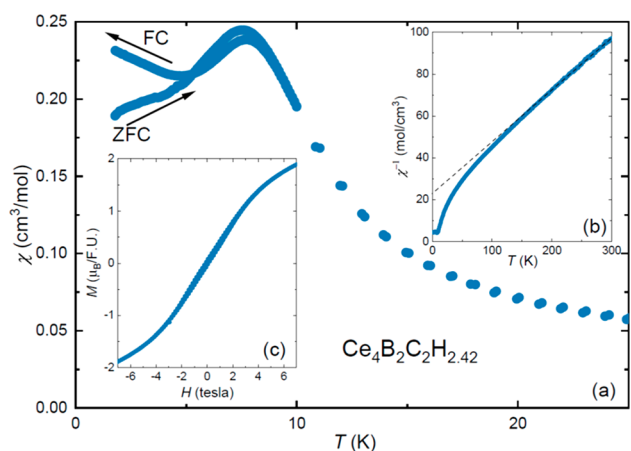


Figure 4. (a) DC magnetic susceptibility $\chi = M/H$ vs temperature T collected in a magnetic field $H = 2000$ Oe for $\text{Ce}_4\text{B}_2\text{C}_2\text{H}_{2.42}$. (b) The inverse magnetic susceptibility $\chi^{-1}(T)$. The straight dotted line is a Curie–Weiss fit to the data, as described in the text. (c) Magnetization data collected at 1.8 K.

Curie–Weiss behavior ($\chi(T) = C/T - \Theta$), yielding an effective magnetic moment $\mu_{\text{eff}} = 2.72 \mu_B/\text{Ce}$ and a Weiss constant $\Theta = -81$ K. The value of μ_{eff} is slightly enhanced by comparison to the expected value for trivalent cerium ($\mu_{\text{eff}} = 2.52 \mu_B$) but is within the range of experimental values that are seen for other cerium-based intermetallics.^{12,13} We also note that the large and negative Weiss temperature is consistent with cerium-based intermetallics with hybridization between the f - and conduction electron states. $\chi(T)$ begins to deviate from the Curie–Weiss temperature dependence below 150 K, as is often seen when the crystal electric field splits the trivalent cerium Hund’s rule multiplet, and the higher energy states are depopulated with decreasing temperature. Finally, complicated behavior is seen at low temperatures, where there is an obvious decrease in χ near $T_{\text{mag}} = 7.7$ K due to magnetic ordering. There is a small hysteresis between the zero field cooled (ZFC) and field cooled (FC) data and in the $M(H)$ curve at 1.8 K, indicating that the ordering involves (i) the formation of domains and (ii) that while the ordering primarily tends to decrease χ as would be expected for an antiferromagnet, there is a quasi-ferromagnetic component as well. This may indicate the formation of a canted spin configuration, ferrimagnetism, or magnetic frustration. Spin glass behavior was ruled out as a possibility in this sample, as AC susceptibility measurements did not show a change in either transition temperature with a change in frequency.

XPS Studies. Additional information regarding the cerium valence of $\text{Ce}_4\text{B}_2\text{C}_2\text{H}_{2.42}$ was sought using XPS measurements. The Ce 3d core-line spectrum for $\text{Ce}_4\text{B}_2\text{C}_2\text{H}_{2.42}$ is shown in Figure 5; it features peaks and satellites typical for Ce^{3+}

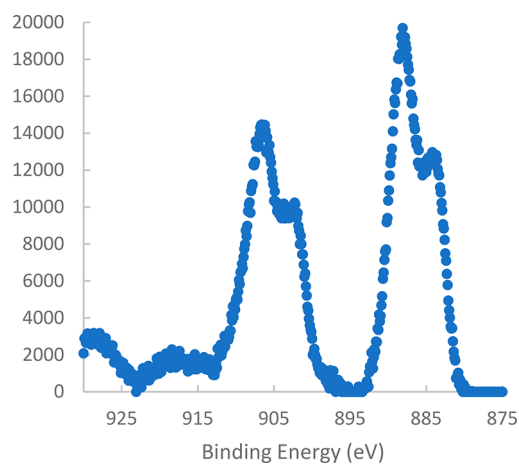


Figure 5. XPS data for $\text{Ce}_4\text{B}_2\text{C}_2\text{H}_{2.42}$.

compounds and is very similar to data reported for trivalent cerium compounds such as CeFeAsO .³⁹ The presence of Ce^{4+} is most easily confirmed by the presence of a sharp peak at 918 eV, which is absent in the spectrum.

Electrical Transport and Heat Capacity Measurements. The magnetic susceptibility and XPS data indicate that the cerium in $\text{Ce}_4\text{B}_2\text{C}_2\text{H}_{2.42}$ is trivalent near room temperature, which potentially sets the stage for complex phenomena such as fluctuating valence, Kondo lattice behavior, or heavy fermion effects, as has been reported for many Ce-based compounds such as $\text{CePt}_4\text{Ge}_{12}$ and several ternary phases in the Ce/Ru/Mg family.^{17,18,40,41} The temperature-dependent heat capacity and electrical resistivity are shown in Figure 6. As shown in panel a, C/T initially

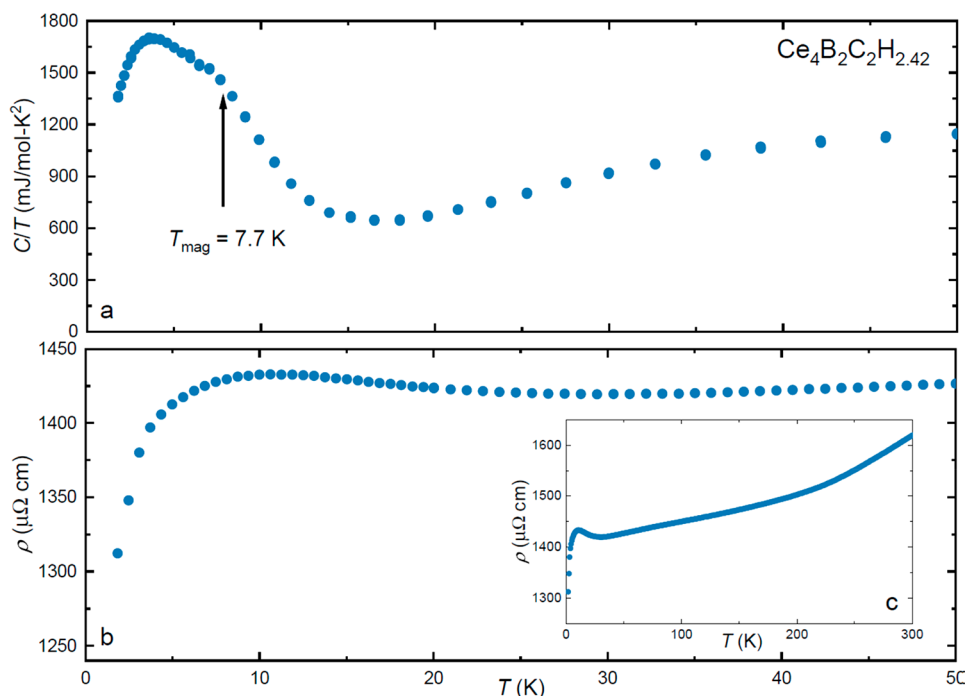


Figure 6. (a) The temperature T dependence of the heat capacity C/T for $\text{Ce}_4\text{B}_2\text{C}_2\text{H}_{2.42}$. The ordering temperature T_{mag} determined from magnetic susceptibility measurements is indicated with an arrow. (b) The low temperature electrical resistivity $\rho(T)$. (c) $\rho(T)$ over a broad temperature range.

decreases with decreasing T in a manner that is consistent with a typical Debye function representing the lattice heat capacity. Near 15 K, C/T deviates from this behavior by gradually increasing with decreasing T . This is likely due to the onset of magnetic fluctuations that precede the magnetic ordering seen in $\chi(T)$ at $T_{\text{mag}} = 7.7$ K. At T_{mag} , there is a shoulder in C/T that is followed by a maximum near 3.7 K. These features show that the magnetic entropy is spread over a broad temperature range that extends well above the magnetic ordering temperature. This may suggest that the magnetism is frustrated or that crystallographic disorder (such as the partial occupancy of the octahedral hydride site) impacts the magnetic ordering. After this C/T begins to drop to smaller values but only reaches $1353 \text{ mJ/mol}\cdot\text{K}^2$ at 1.8 K, indicating a substantial residual magnetic heat capacity. Because of the feature at 7.7 K caused by the magnetic ordering, it is difficult to obtain a value for the electronic coefficient of the heat capacity from the expression $C/T = \gamma + \beta T^2$. However, on the basis of the large value of C/T at 1.8 K, we infer that this compound may exhibit heavy fermion behavior similar to what is seen in other Ce-based intermetallics. Further insight is gained from the electrical resistivity measurements (Figure 6b,c), which show that $\rho(T)$ is large and weakly temperature dependent. This may also indicate that there is substantial disorder scattering. At low temperatures, $\rho(T)$ evolves through a broad minimum near 25–30 K and is weakly reduced upon entering the ordered state.

CONCLUSION

The synthesis and characterization of $\text{Ce}_4\text{B}_2\text{C}_2\text{H}_{2.42}$ show the potential for the flux growth of complex intermetallics containing hydride interstitials. While the initial discovery of this phase was due to the presence of impurities, the ability to replicate it by deliberate addition of a reactant that generates hydrogen in situ presents a new avenue for the isolation of

complex metal hydrides. This was also demonstrated by our recent report on the flux synthesis of $\text{La}_{15}(\text{FeC}_6)_4\text{H}$.⁴² Further flux reactions using anthracene are underway to investigate the growth of other intermetallic compounds that might be stabilized by the presence of interstitial hydrides, such as other analogues of $\text{R}_4\text{B}_2\text{C}_2\text{H}_x$ ($\text{R} = \text{La}, \text{Pr}, \text{Nd}$). Magnetic susceptibility data for $\text{Ce}_4\text{B}_2\text{C}_2\text{H}_{2.42}$ show a broad, possibly frustrated antiferromagnetic transition at 7.7 K; heat capacity and resistivity studies show deviations starting at higher temperatures, possibly due to magnetic fluctuations preceding the ordering transition. This indicates that the partial occupancy of the octahedral hydride sites has a notable scattering effect and may also modify the magnetic coupling in the surrounding cerium ions. It would be of interest to explore deliberate modification of this occupancy (e.g., synthesizing $\text{Ce}_4\text{B}_2\text{C}_2\text{H}_x$ with $x = 2$ or 3) to tailor the behavior of this material.

ASSOCIATED CONTENT

Accession Codes

CCDC 2086224 contains the supplementary crystallographic data for this paper. These data can be obtained free of charge via www.ccdc.cam.ac.uk/data_request/cif, or by emailing data_request@ccdc.cam.ac.uk, or by contacting The Cambridge Crystallographic Data Centre, 12 Union Road, Cambridge CB2 1EZ, UK; fax: +44 1223 336033.

AUTHOR INFORMATION

Corresponding Author

Susan E. Lattner – Department of Chemistry and Biochemistry, Florida State University, Tallahassee, Florida 32306, United States; orcid.org/0000-0002-6146-5333; Email: slattner@fsu.edu

Authors

Mary B. Hertz – Department of Chemistry and Biochemistry, Florida State University, Tallahassee, Florida 32306, United States

Ryan Baumbach – Department of Physics and National High Magnetic Field Laboratory, Tallahassee, Florida 32310, United States

Xiaoping Wang – Neutron Scattering Division, Oak Ridge National Laboratory, Oak Ridge, Tennessee 37831, United States; orcid.org/0000-0001-7143-8112

Complete contact information is available at:
<https://pubs.acs.org/10.1021/acs.cgd.1c00521>

Notes

The authors declare no competing financial interest.

ACKNOWLEDGMENTS

This research was supported by the Division of Materials Research of the National Science Foundation (Grant DMR-18-08471). This research used resources in the X-ray Crystallography Center at the FSU Department of Chemistry and Biochemistry (FSU075000XRAY). This work made use of SEM-EDS equipment of the Biological Sciences Imaging Resource (BSIR) in the Florida State University Department of Biology and XPS equipment of the Condensed Matter and Material Physics (CMMP) group in the Florida State University Department of Physics; we thank Dr. Eric Lochner for guidance with these instruments. The magnetization and electrical resistivity measurements were performed at the National High Magnetic Field Laboratory, which is supported by National Science Foundation Cooperative Agreement No. DMR-1644779 and the State of Florida. Neutron diffraction data were collected at TOPAZ (BL-12) at Oak Ridge National Laboratory's Spallation Neutron Source, a DOE Office of Science User Facility.

REFERENCES

- (1) Babizhetskyy, V.; Simon, A.; Mattausch, H.; Hiebl, K.; Zheng, C. New ternary rare-earth metal boride carbides $R_{15}B_4C_{14}$ ($R = Y, GdLu$) containing BC_2 units: Crystal and electronic structures, magnetic properties. *J. Solid State Chem.* **2010**, *183*, 2343–2351.
- (2) Mattausch, H.; Simon, A.; Felser, C.; Dronskowski, R. $La_9Br_5(CBC)_3$: A New Superconductor. *Angew. Chem., Int. Ed. Engl.* **1996**, *35*, 1685–1687.
- (3) Mattausch, H.; Simon, A. Bromides of Rare Earth Metal Boride Carbides—A System of Building Blocks. *Angew. Chem., Int. Ed. Engl.* **1995**, *34*, 1633–1635.
- (4) Mattausch, H.; Oeckler, O.; Simon, A. B and B–C as interstitials in reduced rare earth halides. *Inorg. Chim. Acta* **1999**, *289*, 174–190.
- (5) Fadel, L.; Zouchoune, F.; Zouchoune, B.; Halet, J.; Saillard, J. Bonding Analysis in Solid State Compounds: Boron Carbon of Rare Earth Metals. *Courrier du Savoir* **2003**, *3*, 99–102.
- (6) Bauer, J.; Bars, O. The ordering of boron and carbon atoms in the LaB_2C_2 structure. *Acta Crystallogr., Sect. B: Struct. Crystallogr. Cryst. Chem.* **1980**, *36*, 1540–1544.
- (7) Zhou, S.; Mishra, T.; Lyman, D.; Tucker, P.; Lattner, S. E. New cerium cobalt borocarbide synthesized from eutectic metal flux mixture. *Inorg. Chem. Front.* **2017**, *4*, 450–455.
- (8) Zhou, S.; Lattner, S. E. $Nd_8Co_{4-x}Al_xGe_2C_3$: A case study in flux growth of lanthanide-rich intermetallics. *J. Solid State Chem.* **2016**, *236*, 159–165.
- (9) Zhou, S.; Lattner, S. E. Flux growth and magnetic properties of rare earth cobalt germanide, $RE_6Co_5Ge_{1+x}Al_{3-x}$ ($RE = Pr, Nd$; $x \approx 0.8$). *J. Solid State Chem.* **2016**, *238*, 189–194.
- (10) Benbow, E. M.; Dalal, N. S.; Lattner, S. E. Spin Glass Behavior of Isolated, Geometrically Frustrated Tetrahedra of Iron Atoms in the Intermetallic $La_2Fe_8Sn_7C_{12}$. *J. Am. Chem. Soc.* **2009**, *131*, 3349–3354.
- (11) Lynn, J. W.; Skanthakumar, S.; Huang, Q.; Sinha, S. K.; Hossain, Z.; Gupta, L. C.; Nagarajan, R.; Godart, C. Magnetic order and crystal structure in the superconducting RNi_2B_2C materials. *Phys. Rev. B: Condens. Matter Mater. Phys.* **1997**, *55*, 6584–6598.
- (12) Stewart, G. R. Heavy Fermion Systems. *Rev. Mod. Phys.* **1984**, *56*, 755.
- (13) Stewart, G. R. Non-Fermi-liquid behavior in d - and f -electron metals. *Rev. Mod. Phys.* **2001**, *73*, 797.
- (14) Moshopoulou, E. G.; Sarrao, J. L.; Pagliuso, P. G.; Moreno, N. O.; Thompson, J. D.; Fisk, Z.; Ibberson, R. M. Comparison of the crystal structure of the heavy-fermion materials $CeCoIn_5$, $CeRhIn_5$ and $CeIrIn_5$. *Appl. Phys. A: Mater. Sci. Process.* **2002**, *74*, s895–s897.
- (15) Rauchsvalbe, U.; Gottwick, U.; Ahlheim, U.; Mayer, H. M.; Steglich, F. Investigation of new lanthanum-, cerium- and uranium-based ternary intermetallics. *J. Less-Common Met.* **1985**, *111*, 265–275.
- (16) Kratochvilova, M.; Dusek, M.; Uhlirva, K.; Rudajevova, A.; Prokleska, J.; Vondrackova, B.; Custers, J.; Sechovsky, V. Single crystal study of the layered heavy fermion compounds Ce_2PdIn_8 , Ce_3PdIn_{11} , Ce_2PtIn_8 and Ce_3PtIn_{11} . *J. Cryst. Growth* **2014**, *397*, 47–52.
- (17) Löhneysen, H. v.; Rosch, A.; Vojta, M.; Wölfle, P. Fermi-liquid instabilities at magnetic quantum phase transitions. *Rev. Mod. Phys.* **2007**, *79*, 1015–1075.
- (18) Pfeleiderer, C. Superconducting phases of f -electron compounds. *Rev. Mod. Phys.* **2009**, *81*, 1551.
- (19) Kanatzidis, M. G.; Pöttgen, R.; Jeitschko, W. The Metal Flux: A Preparative Tool for the Exploration of Intermetallic Compounds. *Angew. Chem., Int. Ed.* **2005**, *44*, 6996–7023.
- (20) Jeevan, H. S. Crystal Growth and Investigation of $CeCu_2Si_2$ and $YbRu_2Ge_2$: Competition/Co-existence of Superconducting, Dipolar and Quadrupolar order. Crystal Growth and Investigation of $CeCu_2Si_2$ and $YbRu_2Ge_2$: Competition/Co-existence of Superconducting, Dipolar and Quadrupolar order, 2010.
- (21) Steglich, F.; Aarts, J.; Bredl, C. D.; Lieke, W.; Meschede, D.; Franz, W.; Schäfer, H. Superconductivity in the Presence of Strong Pauli Paramagnetism: $CeCu_2Si_2$. *Phys. Rev. Lett.* **1979**, *43*, 1892–1896.
- (22) Lang, D. A.; Zaikina, J. V.; Lovingood, D. D.; Gedris, T. E.; Lattner, S. E. Ca_2LiC_3H : A new complex carbide hydride phase grown in metal flux. *J. Am. Chem. Soc.* **2010**, *132*, 17523–17530.
- (23) Lang, D. A.; Lattner, S. E. Two Germanite Hydride Phases Grown in Calcium-Rich Flux: Use of Interstitial Elements for Discovery of New Phases. *Eur. J. Inorg. Chem.* **2011**, *2011*, 4006–4011.
- (24) Dickman, M. J.; Schwartz, B. V. G.; Lattner, S. E. Low-Dimensional Nitridosilicates Grown from Ca/Li Flux: Void Metal $Ca_8In_2SiN_4$ and Semiconductor Ca_3SiN_3H . *Inorg. Chem.* **2017**, *56*, 9361–9368.
- (25) SAINT; Bruker, 2012.
- (26) SADABS; Bruker, 2001.
- (27) Sheldrick, G. M. Crystal structure refinement with SHELXL. *Acta Crystallogr., Sect. C: Struct. Chem.* **2015**, *71*, 3–8.
- (28) Xue, Z.; Ramirez-Cuesta, A.; Brown, C.; Calder, S.; Cao, H.; Chakoumakos, B.; Daemen, L.; Huq, A.; Kolesnikov, A.; Mamontov, E.; Podlesnyak, A.; Wang, X. P. *Eur. J. Inorg. Chem.* **2019**, *2019*, 1065–1089.
- (29) Zikovsky, J.; Peterson, P. F.; Wang, X. P.; Frost, M.; Hoffmann, C. CrystalPlan: an experiment-planning tool for crystallography. *J. Appl. Crystallogr.* **2011**, *44*, 418–423.
- (30) Arnold, O.; Bilheux, J. C.; Borreguero, J. M.; Buts, A.; Campbell, S. I.; Chapon, L.; Doucet, M.; Draper, N.; Ferraz Leal, R.; Gigg, M. A.; Lynch, V. E.; Markvardsen, A.; Mikkelsen, D. J.; Mikkelsen, R. L.; Miller, R.; Palmen, K.; Parker, P.; Passos, G.; Perring, T. G.; Peterson, P. F.; Ren, S.; Reuter, M. A.; Savici, A. T.; Taylor, J. W.; Taylor, R. J.; Tolchenov, R.; Zhou, W.; Zikovsky, J.

Mantid—Data analysis and visualization package for neutron scattering and μ SR experiments. *Nucl. Instrum. Methods Phys. Res., Sect. A* **2014**, *764*, 156–166.

(31) Schultz, A. J.; Jørgensen, M. R. V.; Wang, X.; Mikkelsen, R. L.; Mikkelsen, D. J.; Lynch, V. E.; Peterson, P. F.; Green, M. L.; Hoffmann, C. M. Integration of neutron time-of-flight single-crystal Bragg peaks in reciprocal space. *J. Appl. Crystallogr.* **2014**, *47*, 915–921.

(32) Jepsen, O.; Burkhardt, A.; Andersen, O. K. *The Program TB-LMTO-ASA, version 4.7*; Max-Planck Institut für Festkörperforschung: Stuttgart, Germany, 2000.

(33) Blöchl, P. E.; Jepsen, O.; Andersen, O. K. Improved tetrahedron method for Brillouin-zone integrations. *Phys. Rev. B: Condens. Matter Mater. Phys.* **1994**, *49*, 16223–16233.

(34) Sarussi, D.; Jacob, I.; Bloch, J.; Shamir, N.; Mintz, M. H. The kinetics and mechanism of cerium hydride formation. *J. Alloys Compd.* **1993**, *191*, 91–99.

(35) Babizhetskyy, V.; Köhler, J.; Mattausch, H.; Simon, A. Synthesis, structure and properties of Nd₂BC containing the trans-dibora-(1,3)-butadiene [C=B–B=C]⁸⁻ unit. *Zeitschrift für Kristallographie* **2011**, *226*, 93–98.

(36) Kost, M. E.; Gol'der, G. A. Crystal structure and density of cerium hydrides. *Zh. Neorg. Khim.* **1959**, *4*, 1488–1490.

(37) Hill, H. H. Early Actinides: The Periodic System's *f*-electron Transition Metal Series. *Nucl. Met., Met. Soc. AIME* **1970**.17219

(38) Rambabu, D.; Malik, S. K. Magnetization Studies of CeCu₂Si_{2-x}Ge_x Alloys. In *Theoretical and Experimental Aspects of Valence Fluctuations and Heavy Fermions*; Gupta, L. C., Malik, S. K., Eds.; Springer US: Boston, MA, 1987; pp 409–412.

(39) Blanchard, P. E. R.; Cavell, R. G.; Mar, A. Effects of rare-earth substitution in the oxyarsenides REFeAsO (RE=Ce, Pr, Nd, Sm, Gd) and CeNiAsO by X-ray photoelectron and absorption spectroscopy. *J. Solid State Chem.* **2010**, *183*, 1477–1483.

(40) Gumeniuk, R.; Kvashnina, K. O.; Schnelle, W.; Nicklas, M.; Borrmann, H.; Rosner, H.; Skourski, Y.; Tsirlin, A. A.; Leithe-Jasper, A.; Grin, Y. Physical properties and valence state of cerium in the filled skutterudite CePt₄Ge₁₂. *J. Phys.: Condens. Matter* **2011**, *23*, 465601.

(41) Matar, S. F.; Chevalier, B.; Pottgen, R. Intermediate cerium valence intermetallics Ce₄RuMg, Ce₂₃Ru₇Mg₄, CeRu₂Mg₅, and Ce₂Ru₄Mg₁₇: Electronic structures and chemical bonding from DFT. *Intermetallics* **2012**, *31*, 88–93.

(42) Engstrand, T. O.; Cope, E. M.; Vasquez, G.; Haddock, J. W.; Hertz, M. B.; Wang, X.; Lattner, S. E. Flux synthesis of a metal carbide hydride using anthracene as a reactant. *Inorg. Chem.* **2020**, *59*, 11651–11657.